Biomedical Signal Processing and Control 49 (2019) 473–482

Contents lists available at ScienceDirect

Biomedical Signal Processing and Control

journal homepage: www.elsevier.com/locate/bspc

Automated quantification of immunomagnetic beads and leukemia cells from optical microscope images

Fatma Uslu[a], Kutay Icoz[a,b,c,*], Kasim Tasdemir[c], Bulent Yilmaz[a,b,c]

[a] BioMINDS (Bio Micro/Nano Devices and Sensors) Lab, Electrical and Electronics Engineering Department, Abdullah Gül University, Kayseri, 38080, Turkey
[b] Bioengineering Department, Abdullah Gül University, Kayseri, 38080, Turkey
[c] Computer Engineering Department, Abdullah Gül University, Kayseri, 38080, Turkey

ARTICLE INFO

Article history:
Received 9 July 2018
Received in revised form 1 November 2018
Accepted 4 January 2019
Available online 8 January 2019

Keywords:
Leukemia cells
Image-processing
Bright-field optical microscopy
Machine learning
Immunomagnetic beads
Support vector machines

ABSTRACT

Quantification of tumor cells is crucial for early detection and monitoring the progress of cancer. Several methods have been developed for detecting tumor cells. However, automated quantification of cells in the presence of immunomagnetic beads has not been studied. In this study, we developed computer vision based algorithms to quantify the leukemia cells captured and separated by micron size immunomagnetic beads. Color, size based object identification and machine learning based methods were implemented to quantify targets in the images recorded by a bright field microscope. Images acquired by a 40× or a 20× objective were analyzed, the immunomagnetic beads were detected with an error rate of 0.0171 and 0.0384 respectively. Our results reveal that the proposed method attains 91.6% precision for the 40× objective and 79.7% for the 20× objective. This algorithm has the potential to be the signal readout mechanism of a biochip for cell detection.

1. Introduction

Cancer is the second leading cause of death in the United States and expected to surpass heart diseases in the next five years [1]. Early detection of tumor cells and quantifying the tumor cells during the therapy are crucial for a successful treatment. There are different treatments for cancer patients such as surgery, drug therapy (chemotherapy), transplantation, radiation treatment and immunotherapy. Among these methods chemotherapy is a widely used first line treatment for leukemia but its results differ from patient to patient [2]. Some of the treated patients with chemotherapy achieve remission whereas the cancer cells of some patients are resistant to treatment. The resistant cancer cells (blast cells) can cause relapses and repeat the cancer known as minimal residual disease (MRD) [3]. Mainly two approaches; immunological assays and polymerase chain reaction (PCR)-based molecular assays have been developed for the detection and characterization of circulating tumor cells, disseminated tumor cells [4], and MRD [3].

As an alternative to bench top instruments, novel microfluidics and lab-on-a-chip systems have been demonstrated to capture, isolate and count the tumor cells. Tumor cell size-based, microfabricated uniform single layer [5] and multi-layer micro-filters [6], antibody coated micro-posts in a microfluidic channel [7], immunomagnetic bead-based isolation and magnetic fixation in a chip [8] are among the promising methods. In order to characterize and enumerate tumor cells, optical microscope, phase contrast, and immunofluorescence images have been used to analyze samples in lab-on-a-chip devices [6–8]. Incorporating immunomagnetic beads have prominent features that make them favorable for lab-on-a-chip systems: 1) immunomagnetic beads are coated with receptors to capture the target molecules and 2) external magnetic fields can be applied to move and immobilize immunomagnetic beads. As demonstrated in [8], magnetic beads conjugated with various antibodies (anti-EpCAM, anti-EGFR and anti-CEA) to capture breast cancer cells (MCF-7), non-small cell lung cancer (NSCLC) cells and pancreatic cancer (PANC) cells respectively from blood samples. The loaded and unloaded immunomagnetic beads were flowed through a size-based micro-filter to clear out the unloaded immunomagnetic beads. The loaded immunomagnetic beads were captured on the chip surface by applying an external magnetic field. Then, cells on the chip surface were quantified using the fluorescent images, which requires staining steps and a bench top fluorescent microscope. A mobile readout method was used for CD^+ lymphocytes. The captured cells by immunomagnetic beads were tagged with anti-CD3 antibody, which was conjugated with horseradish

* Corresponding author at: BioMINDS (Bio Micro/Nano Devices and Sensors) Lab, Electrical and Electronics Engineering Department, Abdullah Gül University, Kayseri, 38080, Turkey.
E-mail address: kutay.icoz@agu.edu.tr (K. Icoz).

https://doi.org/10.1016/j.bspc.2019.01.002
1746-8094/

peroxidase (HPS). The color change was detected using a mobile phone [9].

Fluorescent or HPS labels require using secondary antibodies, which increases the complexity of the process and the cost. Alternative to optical approaches, magnetic readout methods for the biosensors that incorporate immunomagnetic beads have been demonstrated such as magnetoresistive [10,11] and magnetic resonance [12]. Even though these systems can be miniaturized they can only provide cell number data but not shape, size and morphology measurements that image based systems can provide.

Recent autonomous image analysis methods on digital pathology and microscopy images for cell detection and segmentation were extensively reviewed in [13]. Bright-field microscopy is the easiest and the lowest cost method compared to fluorescence [14], phase contrast and electron microscopy. Automated image-processing methods based on thresholding [15] and segmentation [16] algorithms were developed to classify white blood cells and to identify leukocytes. However, all of these methods start with the images of stained cells, because the cell's optical properties make it difficult to detect cells in bright-field images [17]. Immunomagnetically selected carcinoma cells were stained and an automated digital microscopy system including an image processing system collected the images and detected the cells [18]. There are open access software tools ImageJ [19] and CellProfiler [20] to analyze bright field images and measure several cell features. Also, machine learning-based methods have been developed to automatically detect cells from bright-field images [21–23]?. In [21] a high-throughput processing including background correction, identification and object splitting techniques were performed on images that have illumination variations. A support vector machine (SVM) with a training algorithm was formulated to detect unstained living and none-living cells in bright field images [23]. In [22] both adherent and suspension cell lines in bright field microscope images were detected using scale-invariant feature transform (SIFT), random forests and hierarchical clustering.

Even analyzing bright-field microscope images to count cells has been demonstrated, to our best knowledge the enumeration of immunomagnetic beads and leukemia cells have not been reported.

In this manuscript we introduce an automated quantification method to quantify immunomagnetic beads and suspended leukemia cells in the images acquired from a bright-field microscope using 20× and 40× objectives. The immunomagnetic beads are conjugated with anti-human CD19 antibodies that specifically bind to the B-type leukemia cells.

We have utilized image processing and computer vision algorithms benefiting from color, size and distinct pattern features of immunomagnetic beads and cells to detect and quantify cells.

Our ultimate goal is to develop a microfluidic platform (MRD Biochip) for monitoring MRD. In such a platform immunomagnetic beads will be used to capture and separate target cells and image processing algorithms together with machine learning methods will form the signal readout mechanism. This work investigates the signal readout mechanism of the MRD biochip which is under development.

2. Materials and methods

2.1. Immunomagnetic capture of B lymphoblast cells

Immunomagnetic beads of 4.5 μm in diameter coupled with monoclonal anti- CD19-human antibody purchased from ThermoFisher (Waltham, MA), B lymphoblast cells CCRF-SB purchased from ATCC (Rockville, MD), cell counting was performed using Muse Cell Analyzer (Millipore, Billerica, MA) and manually using a Neubauer Chamber (Sigma-Aldrich, St. Louis, MO). The B lymphoblast cell culture was grown in a flask and kept in the incubator in a constant temperature of 37 °C with 5% constant CO_2 flow. The procedure suggested by Thermo-Fisher was followed to bind immunomagnetic beads to the cells. The unbound cells washed out using a magnetic separator. The solution containing captured cells and unbound immunomagnetic particles placed on a microscope slide using a pipette.

2.2. Image acquisition and processing

Image acquisition was performed using an optical microscopy system including DS-Ri1 model CCD color camera (Nikon Instruments, Melville, NY). The nominal image size was 3116 × 4076 pixels for images acquired by 20×, and 1920 × 2560 pixels for images acquired by 40× objectives (Supplementary table 1).

Detection and counting algorithms were developed using Matlab (R2016a, The MathWorks, Inc. Natick, MA).

3. Detection of immunomagnetic beads and cells and counting process

In order to detect cells in the microscopic images, computer vision algorithms are employed and automated cell detection and quantification methods for 20× and 40× images are proposed.

The images contain immunomagnetic beads and cells in various shapes and sizes (Fig. 1). Cells in the images might appear as either isolated single cell, covered by beads or smaller fragments. When a cell or cell fragment is not bound by any beads, its boundary and characteristic inner texture can be observed. However, when it is partially covered by one or more beads the bound beads might obstruct some part of the cell boundary. Another case is full coverage of cells by beads. In this case, a cluster of beads appears in the image. Hence, cell-counting process includes all these three cases (Fig. 1).

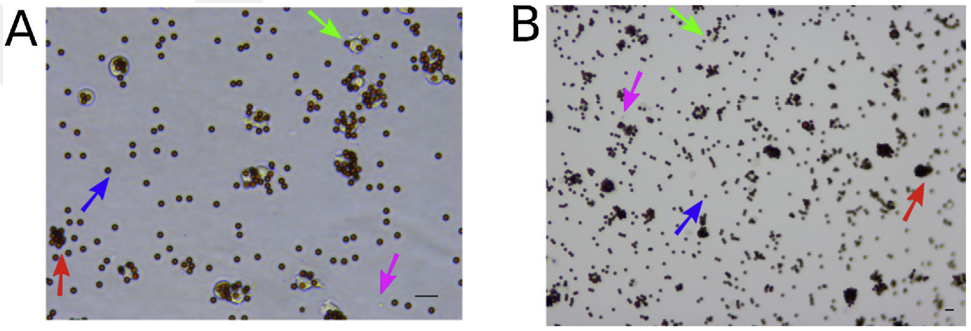

Fig. 1. Typical optical micrographs of cells and beads recorded using A) 40× objective B) 20× objective. Scale bar indicates 20 μm. Blue arrow indicates single beads, pink arrow indicates the cell fragments, green arrow indicates single cell with attached immunomagnetic beads, red arrow indicates fully covered cells with beads as cluster.

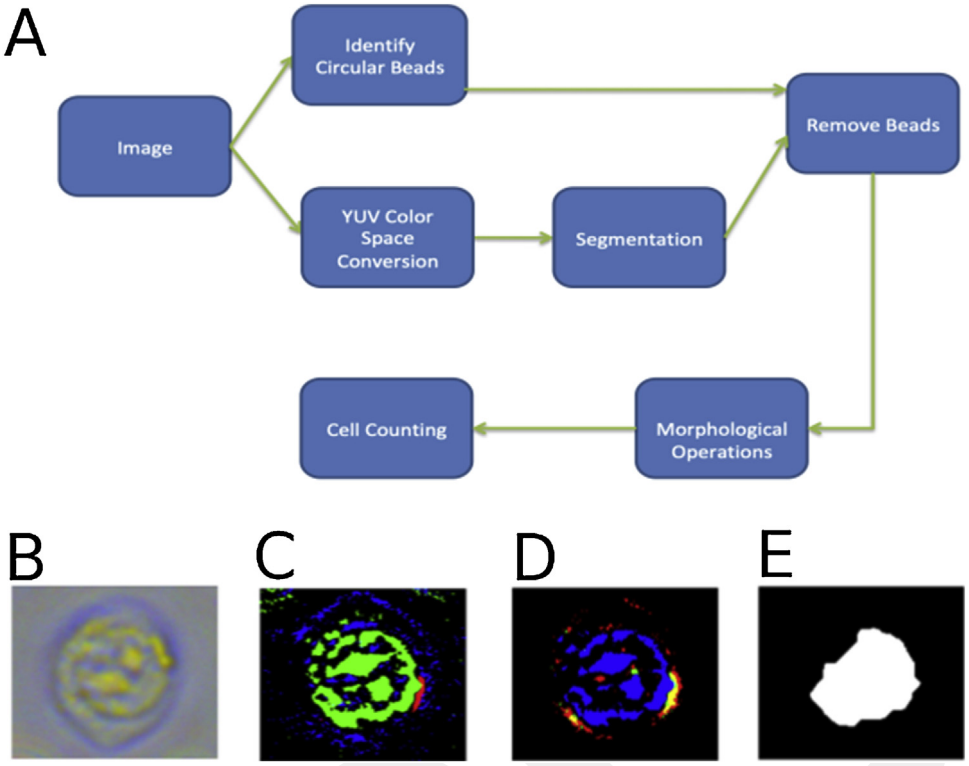

Fig. 2. (A) Flow diagram of cell and bead detection and counting steps for the images recorded using 40× objective, (B) original RGB cell image, (C) YUV thresholded cell image, (D) RGB thresholded cell image, (E) YUV image after morphological operations.

Immunomagnetic beads appear as unbound single beads, as clusters around one cell or bind to cell fragments. As seen in Supplementary table 1, the 40× objective has higher pixel resolution yielded in sharper and clearer images. Therefore, analysis on images acquired by 40× objectives resulted in higher accuracy with less effort compared to analysis on images acquired by 20× objectives.

This study proposes methods for processing images acquired by both objectives. Even though 40× objective has advantages, the field of view of 40× objective is 0.069 mm^2, thus it is slower to analyze a target area compared to 20× objective which has a field of view of 0.278 mm^2. Using real-time image-processing as a signal readout method for a biochip requires scanning a sensor surface in an admissible time. For these reasons this study focuses more on the images acquired by 20× which is time efficient but challenging.

The immunomagnetic bead size variation was neglected since the previous coefficient variation measurements reported a coefficient of variation of 0.024 for the beads produced by the same manufacturer [24]. The uniformity of the immunomagnetic bead size is an advantage for the detection of immunomagnetic beads from the images. Images acquired by 20× objectives may not be clear, the images may have distortions, the edges of the images might be out of focus and the light intensity may not be uniform on the image. Thus machine-learning methods were incorporated to color-based methods to identify cells, immunomagnetic beads and clusters of beads.

3.1. Detection of immunomagnetic beads and cells in images acquired by 40× objective

3.1.1. Counting cells in the images acquired by 40× objective

The main steps of the image-processing algorithm for the images acquired by the 40×objective are depicted in Fig. 2. The same figure also shows the impact of color space conversion from RGB to YUV, and thresholding on these color spaces for a sub-image that contains only one cell.

The images are acquired in raw RGB color space with 0.23 μm/pixel resolution. Since cells are more clearly visible in YUV color space as shown in Fig. 2, RGB images were converted to YUV color space.

Each image can be considered as three separate layers:

$$I = I_{bg} + I_c + I_d \quad (1)$$

where I_{bg}, I_c and I_d represent background, cells and immunomagnetic beads respectively. Cells have a distinct U dominant color, corresponding to more blue color component. To distinguish cells using color feature, a three-channel multilevel thresholding is applied. The binary image of cells layer, B_c, is first estimated by applying a multilevel global threshold (same threshold for all images) as:

$$B_c = \left\{ \begin{array}{l} 1 \; if \; I_Y(x,y) \in T_Y \; and \; I_U(x,y) \in T_U \; and \; I_V(x,y) \in T_V \\ 0 \; if \; otherwise \end{array} \right\} \quad (2)$$

where T_Y, T_U, T_V are color threshold ranges for Y, U and V channels, I_Y, I_U, I_V are Y, U, V channels of the image. This thresholding operation can detect most of the cell fragments but also because the fringing effect around the beads also falls into this color-range. Fortunately, beads are disparately in circular form and have an almost uniform size. In order to eliminate the beads from the cell layer, the beads are found by searching circular objects in an empirically determined size and diameter. Circular objects are detected using Hough transform [25]. After detecting the circular objects, B_d, these objects are removed from the estimated cell layer, B_c, following a dilation and a hole filling operation. This way, the adverse fringing effects of the beads are eliminated in new cell layer estimation $\hat{B}_c$ as in

$$\hat{B}_c = B_c - (B_d \oplus s) \quad (3)$$

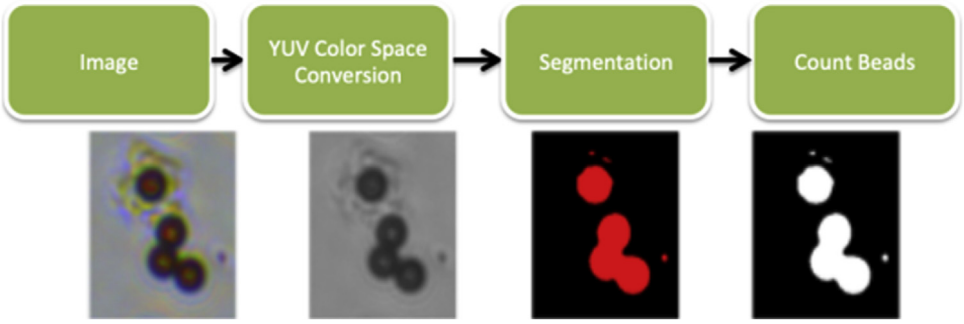

Fig. 3. The flow diagram of the bead detection using Y channel in YUV color space from the images acquired by the 40× objective.

where B_d is the binary image showing beads, $\oplus$ is dilation operation and s is a disc shaped structuring element (SE).

The objects smaller than 1200 pixels are removed. Later closing operation is implemented by using disk shaped SE with radius 20 pixels to combine pixels that are close to each other. After these morphological operations, the objects, which represent the cells are counted.

Since the global threshold was determined as a result of an optimization process and then morphological operations were implemented on the images, this process provided consistent results.

3.1.2. Counting cells in the images acquired by 40× objective

The previous approach (using Hough transform to find circular objects) could find isolated beads. However, bead clusters and overlapping beads still could evade from this method. When several beads overlap, complete circular forms of the beads are hindered (Fig. 3). Therefore, the counting is performed by finding the proportion of pixel area of whole beads to that of a single one.

First, bead clusters are segmented using a thresholding on Y channel. This step does not require any fine tuning because those areas are noticeably darker than the background and the cells. In order to count the number of beads in a cluster, average pixel area of a single bead is determined by finding the median size of all connected components. Pixel areas of clusters are divided by the average pixel area of one single bead.

3.2. Detection of immunomagnetic beads and cells in images acquired by 20× objective

For the quantification of the immunomagnetic beads in the images acquired by 20× objective, the same method developed for 40× objective (Fig. 3) is used. However, cells are not clearly visible in 20× images compared to 40× images. Therefore, further image analysis is performed as follows.

Cells might appear as isolated single cells or fully covered cells. Evidently, detection of clearly visible isolated cells requires a different approach than detection of cells that are fully covered by beads. The reason to that is, when a cell is fully obstructed by beads, its texture, color or edges cannot be used in a detection algorithm. Therefore, the proposed algorithm has two main branches: detection of isolated cells, detection of fully obstructed cells. The flow chart of the algorithm is demonstrated in Fig. 4.

Before presenting the proposed algorithm, it should be noted that in addition to aforementioned difficulties of cell detection in the presence of immunomagnetic beads, 20× images pose further challenges. When the zoom factor halved, sensor noise, lens distortions, non-uniform illumination, softer edges and sensor resolution drastically affect the cell detection performance. Unlike in 40× images, using only color and size-based methods do not produce desirable results in 20× images. Therefore, these images required further analysis.

The first branch of the method aims to segment the isolated cells. It is utilizing machine learning tools and has three stages: preprocessing, feature extraction and learning model construction. In the preprocessing stage, the images are divided into 12 × 12 pixel non-overlapping sub-images. In the experiments, eight 20× full sized images yielded 707,200 sub-images in total. The following feature extraction and machine learning stages are carried out on the sub-images (Supplementary information).

The following 273 features are extracted from each RGB sub-image:

Gray Level Cooccurrence Matrix based (GLCM, 264 features) [26],

Mean, variance and skewness (9 features).

In addition, after converting the RGB sub-image to gray-scale, the following 140 features are extracted:

Histogram of Oriented Gradient (HOG, 81 features) [27,28],

Local Binary Pattern (LBP, 59 features) [29],

In the learning model construction stage, SVM is employed for two-class classification. It was shown that SVM based techniques have improved performance to distinguish unstained viable and not-viable cells [23]. For training and tests the ground truth dataset is constructed by an expert by classifying the sub-images as positive (cell) or negative (non-cell). The ground truth dataset is used in learning process and measuring the effectiveness of the algorithm. Overwhelming majority of the sub-images are negative. This unbalanced dataset leads poor learning performance. Therefore, the dataset is rebalanced before the training by down-sampling the negative set [30]. In order to be sure that the model does not learn photo-specific features, leave-one-image-out approach is used. That is, all sub-images of the current test image are left out from training for the test phase. The system is trained by $N_I - 1$ images and tested on sub-images of a single test image, where N_I is the number of images in the set. In the next round, another test image is picked. This model creation and test operations are performed for N_I times, i.e., repeated for each test image. In total, more than 100,000 sub-images are classified by the system. Performance of the system is measured by average output of all rounds. In each round, optimum values of SVM parameters (Supplementary information) C and γ are found by grid search [23]. Radial basis is selected as the kernel function.

In the second branch of the method, bead clusters are detected. Even though the cells are not visible, clusters can be detected using color-based variations and morphological operations.

First, broken connections of the bead clusters are fixed by a morphological closing operation with a 10 pixel sized disc SE. The bead clusters are usually larger than 400 pixels. Therefore, blobs smaller than 400 pixels are removed and bead cluster detection part is completed.

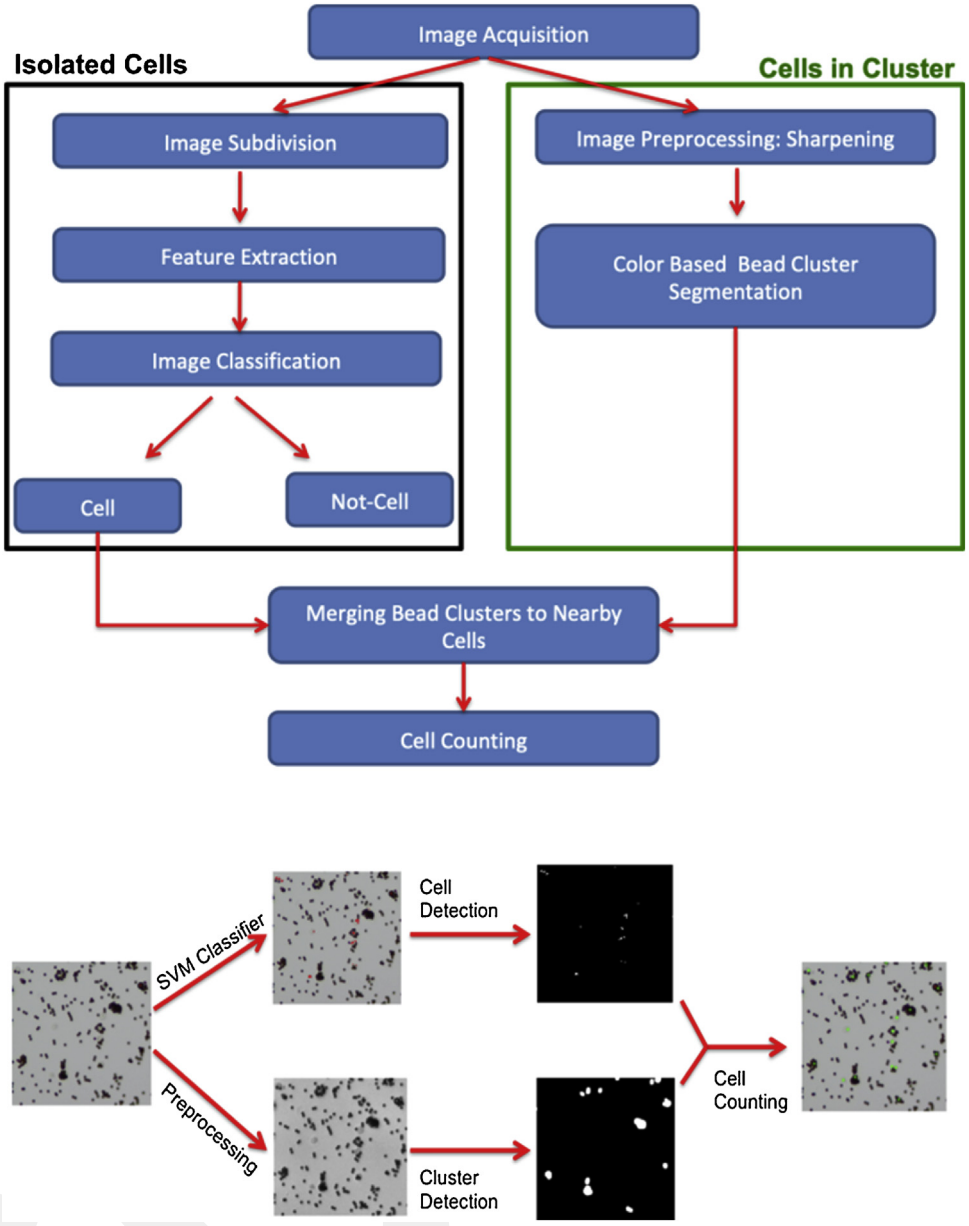

Fig. 4. Flow diagram of cell detection and counting steps for the images recorded using 20× objective.

After completing the two branches shown in Fig. 4, bead clusters and nearby cells are merged because usually partially covered cells protrude below the bead clusters. In order to merge them, first, a Gaussian softening filter with $\sigma = 20$. Then, following a binarization of the image, a morphological closing operation with disc SE = 20 is performed. The algorithm is completed by counting the resulted objects. This gives the number of cells in the image.

4. Results

The images are recorded at different times by different users, thus illumination light variations and focusing problems at the image edges are observed when 20× objective is used. In one image set, sixteen images are acquired by 40× objective and in the other image set 9 images are acquired by 20× objective. For each image set, the number of immunomagnetic beads and cells are counted by the proposed algorithm and compared with the manual counting of an expert. In the following subsections results of the algorithms explained previously are reported for immunomagnetic bead and cell quantification. Fully covered, isolated and partially covered cell detection results and the combination of those three approaches to obtain an overall quantification for the cells are explained.

4.1. Bead quantification

The error rate, E, for bead quantification algorithms is defined as

$$E = \left| \frac{\tilde{N} - N}{N} \right| \tag{4}$$

where N is the number of beads, $\tilde{N}$ is the estimation of N obtained by using the methods depicted in Fig. 3. Error rate is used as an evaluation criteria for bead counting and results for both sets are given in Table 1. The results show that the bead quantification error rate is low for both image sets. That is an expected result because beads are opaque and have a darker texture than the background and cells. However, due to the lower resolution and stronger distor-

Table 1
Average bead counting error rate values for images acquired by 40× and 20× objectives.

	40× Images	20× Images
E	0.0171	0.0384

tion in 20× image set, the results obtained from that set is relatively inferior.

Bead quantification algorithm produces satisfactory results even only size and color features are used. Nevertheless, quantification algorithm of cells is more demanding than that of beads. Cell has a semi-transparent texture which makes it more elusive. Furthermore, accuracy of quantification algorithm for cells is more essential for the users than bead number accuracy. Those requirements and challenges make quantification process lengthier.

4.2. Cell quantification

For evaluating the performances of the algorithms, True Positive (TP), False Positive (FP), and False Negative (FN) values are determined and precision, recall, specificity, F-measure [31], false negative rate [15] and detection error [17] were calculated (Supplementary information).

Typical images acquired by 40× objective Fig. 5 (top-row) and the detected cells are labeled with green star shaped markers by the algorithm in the Fig. 5 (bottom row). The detection of cells and immunomagnetic beads in the images acquired by 40× objective was relatively easy in terms of number of steps carried out by the algorithm and more accurate results obtained compared to the results for the images acquired by the 20× objective.

To visually investigate the performance of the algorithm for cell detection, we compared the images resulted in the lowest precision (image 9) and the highest precision (image 7). The images with highest precision are clear, uniform and the light variations are minimum (Fig. 6, right column).

However the image with the lowest precision has blurry edges (Fig. 6, left column) causing false positives and thus decreasing the precision. In order to show the image quality on the precision, the blurry edges of the lowest precision image was cropped and precision was calculated again (Fig. 7).

By removing the blurry edges precision was increased from 0.54 to 0.85 and detection error was improved from 0.34 to 0.23 (Table 2).

Cropping and leaving the problematic region of the image out significantly increases the detection performance but for the practical reasons, the proposed algorithm analyses whole image and leverages image processing tools to mitigate the problem.

Cells may appear in various forms. We categorized cell appearances into three forms: isolated, partially or fully covered by immunomagnetic beads because each appearance has an unlike and distinct texture in term of image processing. Each category, hence, is analyzed separately. Those separate analyze results are later combined to obtain total number of cells. In the following sections, the results obtained for each category is given for 20× images.

4.2.1. Fully covered cell detection in 20× objectives

One common form of a cell is to appear as cluster of beads. When many immunomagnetic beads are bond to a single cell, the cell looks fully covered by them. Actual texture of the cell is usually concealed but bead clusters are indicators of obscured cells. Therefore, numbers of bead clusters are counted as cells. Nevertheless, bead and bead cluster detection methods proposed have distinct purposes and the terms *bead* and *bead cluster* should not be confused. This section demonstrates the test results for fully covered cell (bead cluster) detection algorithm presented in Fig. 4.

The results of the bead cluster detection algorithm are presented for each image in Supplementary table 3. For the images acquired by 20× an average of 45.7 out of average 58.3 bead clusters were correctly and 12.5 were incorrectly detected from the whole data set. As it is shown in the table, the average precision and F-measure are higher than 80% while recall measure is higher than 94%. Higher recall indicates that most of the bead clusters are identified correctly and there are low numbers of missed detections. However, the precision which is 14% lower than recall indicates that some objects in the image (mostly the ones in the out of focus region) are wrongly identified as bead cluster. For instance, for image 3 which has blurry and out of focus corners, false positive measure is 24 where true positive measure is 55. Unlike image 3, image 4 has a clearer and in focus corners. As a result, the algorithm has 32 true and 2 false positives for cluster detection.

Another challenge for this part is to decide on bead cluster size of how many beads indicate an underlying cell. In this experiment, a minimum bead cluster size is incorporated into the method based on an expert's view.

4.2.2. Isolated and partially covered cell detection in 20× objectives

Isolated or partially covered cells have visible cell texture. Therefore, as described in the Methods section (Fig. 4 SVM branch),

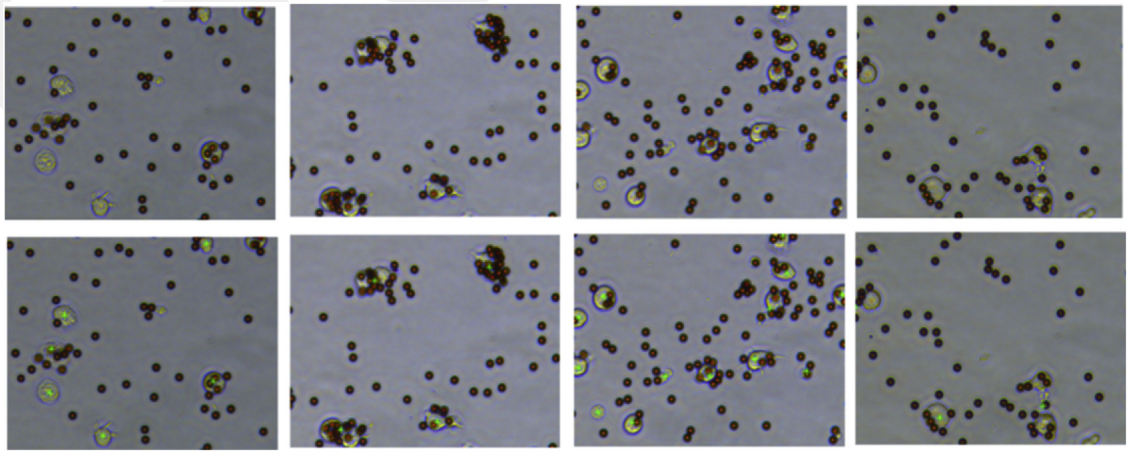

Fig. 5. Original images (top row) and green detection marks for each cell (bottom row) for the 40× objective.

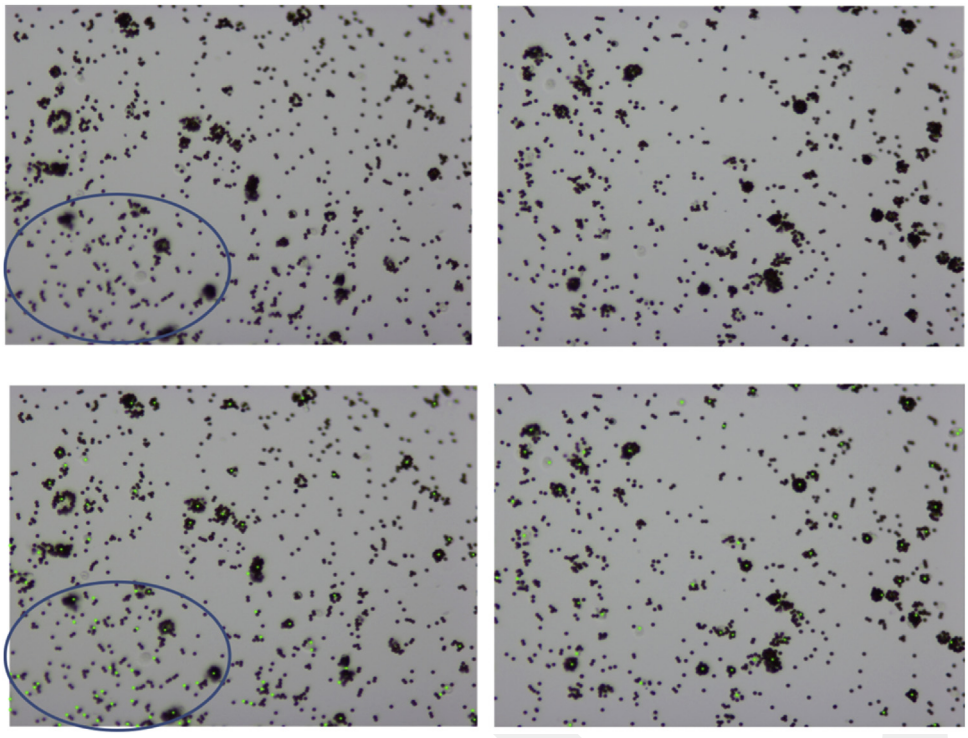

Fig. 6. Comparison of high precision and low precision images. Blue circle indicates the blurry part of the image (top left) and resulted false positives (bottom left).

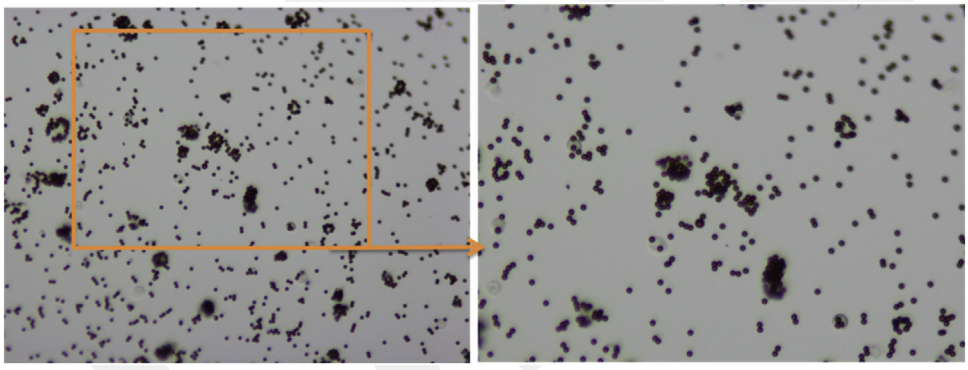

Fig. 7. The impact of image quality on the performance of the image processing algorithm. Original image (image 9) (left), cropped image without blurry part (right).

Table 2
The impact of cropping out the blurry region of the image on the performance of the algorithm.

	Precision	Recall	Specificity	False Negative Rate	F-Measure	Detection Error
Original Image	0.54	0.76	0.99	0.23	0.63	0.34
Excluding the Blurry region	0.85	0.68	0.99	0.32	0.75	0.23

features are extracted from the cell images and trained by SVM to recognize those textures.

However, in order to also test other alternative machine learning methods to SVM, neural networks and random forest are used and compared in Weka data mining software [32,33]. Each image was divided into approximately 88,000 overlapping sub-images of size 12×12 pixels and 413 features described in methods section for each sub-image were extracted. A balanced test data was constructed by under sampling the negative set, that is, combining equal number of sub-image features from cell and not cell classes. For each image a test data was generated and tested in Weka. In order to generate a reliable test results, leave-one (image)-out approach was implemented [34]. Sub-images of one test image completely left out from the training. In each train-test cycles, the next image is chosen as the test image so that at the end, all images are used in the test. The results of those test-train cycles are averaged to indicate the overall performance of the algorithm. SVM, Random Forest (RF) and Neural Networks (NN) were compared in Weka software by using the train and test data. The results of machine learning methods for each image are presented in Supplementary table 4.

Supplementary table 5 summarizes the overall performance of different machine learning algorithms. Random forest has the highest accuracy of 87.4% where Neural Network has the lowest, which is 76.6%. However, it should be noted that the Neural Network settings used for this experiment can be

Table 3
Average Cell Detection Performance of the Algorithms.

	40× Images	20× Images
Precision	0.916	0.797
Recall	0.815	0.883
Specificity	0.99	0.99
False Negative Rate	0.184	0.116
F-Measure	0.861	0.833
Detection Error	0.134	0.159

altered to achieve higher accuracies. In this experiment, a Neural Network with 413 input nodes, 208 hidden neurons and 1 hidden layer are used. The data is normalized before the training.

4.2.3. Quantification of all cell forms in 20× objectives

As mentioned earlier, cells might appear in three forms: isolated, partially or fully covered by immunomagnetic beads. In the previous sections, automated recognition of each form is investigated separately. In this section, those three approaches are combined to give an overall quantification for the cells weather or not covered by immunomagnetic beads. The performance of the algorithm (Fig. 4, cell counting step) for each image is given in Supplementary tables 6 and 7.

The Supplementary table 7 has three columns, namely Correctly Marked, Multiple Marked and Missed Detection, for each cell form. When finding the location of a cell, algorithm can point different positions in a cell. Each location is considered as correct as long as it belongs to a cell. However, when counting the cells, those correct locations are considered as mistake since identification of the same cell for multiple times is an error. The column "Multiple Marked" shows how many times a cell is falsely detected more than once.

The Supplementary table 7 shows that cells in the majority of the images are correctly counted with less missed detection and multiple detection errors.

4.2.4. Average cell detection performance of the algorithms for 40× and 20× objectives

In the previous sections, 40× and 20× magnification images are analyzed individually. In Table 3, results for both types of images are summarized. The table shows that detection performances in 40× magnification images are higher than lower resolution counterpart. However, F-Measure, recall and precision values show that the algorithm's performance in 20× images are also satisfactory.

5. Discussion

Cells can be imaged by bright-field, phase contrast, fluorescence or electron microscopy and the images can be processed to detect and quantify cells or to investigate the sub cellular structures [13]. Electron microscopy offer high resolution images for investigating cell structures [35] and also preferred for verification [36]. Fluorescent microscopy requires labeling cells or cell nuclei with markers and automated cell counting algorithms have been developed [37,38]. Bright-field microscopy is the easiest and the lowest cost method compared to fluorescence, phase contrast and electron microscopy because it does not require expensive labeling agents and optics. In the bright-field images cells are almost transparent and the optical properties of cells induce challenges in detection. To visualize and differentiate cells from other types, cells are stained with dyes [39]. In [18] it was reported that cytokeratin positive cells, associated with breast cancer, separated from blood with immunomagnetic beads and immunocytochemically stained for cell detection. In this manuscript we reported cell detection without any staining procedure. In our method, by detecting immunomagnetic beads from the images, immunomagnetic beads served for two purposes inherent cell separation feature and being visual markers for cell detection.

As presented in Table 2, image quality (blurry edges/uneven illumination) has impact on the performance of the detection algorithm. This impact also reported in [21] for bright field images where uneven illuminations corrected using machine learning based approach yielding 82% accuracy in cell detection which is comparable to the results of machine learning methods to detect cells presented in this study (Table 3). In the literature there are studies stating 95% accuracy [40] and 93.4% accuracy [41], 96% precision [42] for detecting cells from microscope images, however these cells are stained with violet color which makes the cells distinctive. In [43], the average accuracy of SVM method for fluorescently labeled cells was reported as 90%, whereas our method resulted in 86.32% including the blurry images (Supplementary table 7).

In [21] both adherent and suspended cells in bright field microscope images were detected using scale-invariant feature transform (SIFT), random forests and hierarchical clustering. 5 images of the cells in suspension were analyzed and a precision of 0.89 for connected component based method and a precision of 0.93 for SIFT based method were reported. In our study B lymphoblast cells are in suspension and for cell detection the average precision for 9 images is 0.797 (20× objective). The images in this study includes not only cells as analyzed in [22] and [23] but also immunomagnetic beads and clusters of immunomagnetic beads which introduces non-uniformities and creates more challenges. We implemented image processing algorithms to solve three problems: bead detection, cluster detection and cell detection without any staining procedure, then combined the results to quantify cells.

As a finding of this manuscript, the quality of images acquired by a 20× objective has significant impact on the performance of the detection algorithm and we plan to maximize the quality of images by standardizing the imaging process for the MRD Biochip such as adding automated illumination and focusing adjustments.

Our image size is 12 Mega pixel and this image size is higher than the previous studies (1M pixel for [22], 2M pixel for [17]. Higher image size introduces unbalanced data to image processing algorithm since illumination variations are high at the corners. A further analysis on reducing the image size and running the algorithms may clarify this issue.

In order to increase the performance of the method presented in this study, images can be preprocessed to alleviate the illumination changes by using a top-hat transformation before segmentation [44]. To reduce the noise, an adaptive local noise reduction filter [45] can be used at the expense of losing some subtle texture of cells. This requires a priory knowledge of noise model at the background. This model can be estimated using histograms of cropped background regions. In feature extraction part, even it is substantially large, feature set can be expanded adding various other features. Feature set size can also be reduced by selecting the most important features or using a dimension reduction approach such as principal component analysis (PCA). Application of PCA on the images of stained cells to investigate the cell phenotype is reported in [46]. In literature it was reported that future reduction in some cases increase accuracy [47–49] or do not change the accuracy but improve processing cost or data storage [50]. We are planning to test feature reduction to test if there is an improvement in the accuracy or processing cost.

Moreover, comparison of machine learning algorithms showed that significant improvements of the accuracy can be attained by picking the right machine learning algorithm. There is a plethora machine learning algorithms each of which has its own parameter sets and settings. For instance, neural networks setting in the experiment was a standard three layer with one hidden layer. Number of layers as well as that of nodes can be increased or different

nonlinear activation functions can be employed. However, each approach requires time consuming rigorous examination. At this point of accuracy levels, authors find it useful to circulate the current findings and to leave the approaches mentioned above for a further study.

6. Conclusion

The proposed algorithm is planned to be used to quantify cells in a biochip. The biochip incorporates immunomagnetic beads for separation of the target B lymphoblast cells. In this study our main goal is to quantify cells and immunomagnetic beads from the images acquired by 40× or 20× objectives. Without cell staining, color-based methods provided over 90% precision for the images acquired by 40× objective. Only color-based methods were not sufficient to detect cells in the images acquired by 20× objective so SVM incorporated with color-based methods to detect cells and clustered or single immunomagnetic beads. The developed methods were tested by measures images precision, recall, specificity, false negative rate, f-measure and detection error rate. The results showed that the image quality has great impact on the performance of the algorithm. The blurry images increase the false positives thus decrease the precision. The highest precision is 094 for the clear image shows the potential of the developed algorithm.

We previously introduced ultra-low cost mobile cell phone microscopy to quantify immunomagnetic bead amounts on microcontact printed lines [51] without using any secondary labels. It is possible to combine machine-learning based image processing algorithms with cell phone microscopy to analyze immunomagnetic-captured cells in biochips for portable on site analyses, which is our next goal.

Acknowledgement

Authors acknowledge The Scientific and Technological Research Council of Turkey (TÜBİTAK) (Project No: 115E020) for financial support.

Appendix A. Supplementary data

Supplementary material related to this article can be found, in the online version, at doi:https://doi.org/10.1016/j.bspc.2019.01.002.

References

[1] R. Siegel, K. Miller, A. Jemal, Cancer statistics, 2015, CA Cancer J. Clin. 65 (2015) 29, http://dx.doi.org/10.3322/caac.21254.
[2] C.E. DeSantis, C.C. Lin, A.B. Mariotto, R.L. Siegel, K.D. Stein, J.L. Kramer, R. Alteri, A.S. Robbins, A. Jemal, Cancer treatment and survivorship statistics, 2014, CA Cancer J. Clin. 64 (2014) 252–271, http://dx.doi.org/10.3322/caac.21235.
[3] M. Hauwel, T. Matthes, Minimal residual disease monitoring: the new standard for treatment evaluation of haematological malignancies? Swiss Med. 144 (2014), http://dx.doi.org/10.4414/smw.2014.13907.
[4] K. Pantel, R.H. Brakenhoff, B. Brandt, Detection, clinical relevance and specific biological properties of disseminating tumour cells, Nat. Rev. Cancer 8 (2008) 329–340, http://dx.doi.org/10.1038/nrc2375.
[5] S. Zheng, H. Lin, J.-Q. Liu, M. Balic, R. Datar, R.J. Cote, Y.-C. Tai, Membrane microfilter device for selective capture, electrolysis and genomic analysis of human circulating tumor cells, J. Chromatogr. A 1162 (2007) 154–161, http://dx.doi.org/10.1016/j.chroma.2007.05.064.
[6] S. Zheng, H.K. Lin, B. Lu, A. Williams, R. Datar, R.J. Cote, Y.C. Tai, 3D microfilter device for viable circulating tumor cell (CTC) enrichment from blood, Biomed. Microdevices 13 (2011) 203–213, http://dx.doi.org/10.1007/s10544-010-9485-3.
[7] S. Nagrath, L.V. Sequist, S. Maheswaran, D.W. Bell, D. Irimia, L. Ulkus, M.R. Smith, E.L. Kwak, S. Digumarthy, A. Muzikansky, P. Ryan, U.J. Balis, R.G. Tompkins, D. a Haber, M. Toner, Isolation of rare circulating tumour cells in cancer patients by microchip technology, Nature 450 (2007) 1235–1239, http://dx.doi.org/10.1038/nature06385.
[8] C.-L. Chang, W. Huang, S.I. Jalal, B.-D. Chan, A. Mahmood, S. Shahda, B.H. O'Neil, D.E. Matei, C.A. Savran, Circulating tumor cell detection using a parallel flow micro-aperture chip system, Lab Chip 15 (2015) 1677–1688, http://dx.doi.org/10.1039/C5LC00100E.
[9] S. Wang, S. Tasoglu, P.Z. Chen, M. Chen, R. Akbas, S. Wach, C.I. Ozdemir, U.A. Gurkan, F.F. Giguel, D.R. Kuritzkes, U. Demirci, Micro-a-fluidics ELISA for rapid CD4 cell count at the point-of-care, Sci. Rep. 4 (2014) 3796, http://dx.doi.org/10.1038/srep03796.
[10] J.C. Rife, M.M. Miller, P.E. Sheehan, C.R. Tamanaha, M. Tondra, L.J. Whitman, Design and performance of GMR sensors for the detection of magnetic microbeads in biosensors, Sens. Actuators A Phys. 107 (2003) 209–218, http://dx.doi.org/10.1016/S0924-4247(03)00380-7.
[11] D.R. Baselt, G.U. Lee, M. Natesan, S.W. Metzger, P.E. Sheehan, R.J. Colton, A biosensor based on magnetoresistance technology, Biosens. Bioelectron. 13 (1998) 731–739, http://dx.doi.org/10.1016/S0956-5663(98)00037-2.
[12] H. Lee, E. Sun, D. Ham, R. Weissleder, Chip-NMR biosensor for detection and molecular analysis of cells, Nat. Med. 14 (2008) 869–874, http://dx.doi.org/10.1038/nm.1711.
[13] F. Xing, L. Yang, Robust nucleus/cell detection and segmentation in digital pathology and microscopy images: a comprehensive review, IEEE Rev. Biomed. Eng. 9 (2016) 234–263, http://dx.doi.org/10.1109/RBME.2016.2515127.
[14] G. Mata, M. Radojević, C. Fernandez-Lozano, I. Smal, N. Werij, M. Morales, E. Meijering, J. Rubio, Automated neuron detection in high-content fluorescence microscopy images using machine learning, Neuroinformatics (2018), http://dx.doi.org/10.1007/s12021-018-9399-4 [Epub ahead of print].
[15] N. Hazwani, A. Halim, M.Y. Mashor, R. Hassan, Automatic blasts counting for acute leukemia based on blood, Int. J. Res. Rev. Comput. Sci. 2 (2011) 971–976.
[16] L. Putzu, G. Caocci, C. Di Ruberto, Leucocyte classification for leukaemia detection using image processing techniques, Artif. Intell. Med. 62 (2014) 179–191, http://dx.doi.org/10.1016/j.artmed.2014.09.002.
[17] A. Georgantzoglou, M.J. Merchant, J.C.G. Jeynes, A.-C. Wéra, K.J. Kirkby, N.F. Kirkby, R. Jena, Automatic cell detection in bright-field microscopy for microbeam irradiation studies, Phys. Med. Biol. 60 (2015) 6289–6303, http://dx.doi.org/10.1088/0031-9155/60/16/6289.
[18] T.E. Witzig, B. Bossy, T. Kimlinger, P.C. Roche, J.N. Ingle, C. Grant, J. Donohue, V.J. Suman, D. Harrington, J. Torre-Bueno, K.D. Bauer, Detection of circulating cytokeratin-positive cells in the blood of breast cancer patients using immunomagnetic enrichment and digital microscopy, Clin. Cancer Res. 8 (2002) 1085–1091.
[19] M.D. Abràmoff, P.J. Magalhães, S.J. Ram, Image processing with imageJ, Biophotonics Int. 11 (2004) 36–41, http://dx.doi.org/10.1117/1.3589100.
[20] A.E. Carpenter, T.R. Jones, M.R. Lamprecht, C. Clarke, I.H. Kang, O. Friman, Da Guertin, J.H. Chang, Ra Lindquist, J. Moffat, P. Golland, D.M. Sabatini, CellProfiler: image analysis software for identifying and quantifying cell phenotypes, Genome Biol. 7 (2006), R100, http://dx.doi.org/10.1186/gb-2006-7-10-r100.
[21] F. Buggenthin, C. Marr, M. Schwarzfischer, P.S. Hoppe, O. Hilsenbeck, T. Schroeder, F.J. Theis, An automatic method for robust and fast cell detection in bright field images from high-throughput microscopy, BMC Bioinformatics 14 (2013) 297, http://dx.doi.org/10.1186/1471-2105-14-297.
[22] F. Mualla, S. Scholl, B. Sommerfeldt, A. Maier, J. Hornegger, Automatic cell detection in bright-field microscope images using sift, random forests, and hierarchical clustering, IEEE Trans. Med. Imaging 32 (2013) 2274–2286, http://dx.doi.org/10.1109/TMI.2013.2280380.
[23] X. Long, L. Cleveland, Y. Lawrence Yao, Automatic detection of unstained viable cells in bright field images using a support vector machine with an improved training procedure, Comput. Biol. Med. 36 (2006) 339–362, http://dx.doi.org/10.1016/j.compbiomed.2004.12.002.
[24] J. Xu, K. Mahajan, W. Xue, J.O. Winter, M. Zborowski, J.J. Chalmers, Simultaneous, single particle, magnetization and size measurements of micron sized, magnetic particles, J. Magn. Magn. Mater. 324 (2012) 4189–4199, http://dx.doi.org/10.1016/j.jmmm.2012.07.039.
[25] M.R.M, M.K. Mohamed Rizon, Haniza Yazid, Puteh Saad, AliYeonMd Shakaff, Abdul Rahman Saad, Masanori Sugisaka, Sazali Yaacob, Object detection using circular hough transform, Am. J. Appl. Sci. 2 (2005) 1606–1609, http://dx.doi.org/10.3844/ajassp.2005.1606.1609.
[26] R.M. Haralick, K. Shanmugam, Textural features for image classification, Syst. Man Cybern. SMC-3 (6) (1973) 610–621, http://dx.doi.org/10.1109/TSMC.1973.4309314.
[27] N. Dalal, B. Triggs, Histograms of oriented gradients for human detection, Proc. - 2005 IEEE Comput. Soc. Conf. Comput. Vis. Pattern Recognition, CVPR 2005 (2005), http://dx.doi.org/10.1109/CVPR.2005.177.
[28] O.L. Junior, D. Delgado, V. Gonçalves, U. Nunes, Trainable classifier-fusion schemes: an application to pedestrian detection, IEEE Conf. Intell. Transp. Syst. Proceedings (2009), http://dx.doi.org/10.1109/ITSC.2009.5309700.
[29] T. Ojala, M. Pietikäinen, T. Mäenpää, Multiresolution gray-scale and rotation invariant texture classification with local binary patterns, IEEE Trans. Pattern Anal. Mach. Intell. 24 (7) (2002) 971–987, http://dx.doi.org/10.1109/TPAMI.2002.1017623.
[30] R. Akbani, S. Kwek, N. Japkowicz, Applying support vector machine to imbalanced datasets, Mach. Learn. Knowl. Discov. Databases (2004) 39–50, doi:10.1.1.102.5233.
[31] R. Kumar, R. Srivastava, S. Srivastava, Detection and classification of Cancer from microscopic biopsy images using clinically significant and biologically interpretable features, J. Med. Eng. 2015 (2015) 1–14, http://dx.doi.org/10.1155/2015/457906.

[32] L. Shamir, J.D. Delaney, N. Orlov, D.M. Eckley, I.G. Goldberg, Pattern recognition software and techniques for biological image analysis, PLoS Comput. Biol. 6 (2010), http://dx.doi.org/10.1371/journal.pcbi.1000974.
[33] A. Sopharak, M.N. Dailey, B. Uyyanonvara, S. Barman, T. Williamson, K.T. Nwe, Y.A. Moe, Machine learning approach to automatic exudate detection in retinal images from diabetic patients, J. Mod. Opt. 57 (2010) 124–135, http://dx.doi.org/10.1080/09500340903118517.
[34] G.B. Junior, S.V. da Rocha, J.D. de Almeida, A.C. de Paiva, A.C. Silva, M. Gattass, Breast cancer detection in mammography using spatial diversity, geostatistics, and concave geometry, Multimed. Tools Appl. (2018) 1–27, http://dx.doi.org/10.1007/s11042-018-6259-z.
[35] D. Ciresan, A. Giusti, L. Gambardella, J. Schmidhuber, Deep neural networks segment neuronal membranes in Electron microscopy images, Nips (2012) 1–9, doi:10.1.1.300.2221.
[36] Y.-C. Chang, C.-Y. Yang, R.-L. Sun, Y.-F. Cheng, W.-C. Kao, P.-C. Yang, Rapid single cell detection of Staphylococcus aureus by aptamer-conjugated gold nanoparticles, Sci. Rep. 3 (2013) 1863, http://dx.doi.org/10.1038/srep01863.
[37] D.A. Van Valen, T. Kudo, K.M. Lane, D.N. Macklin, N.T. Quach, M.M. DeFelice, I. Maayan, Y. Tanouchi, E.A. Ashley, M.W. Covert, Deep learning automates the quantitative analysis of individual cells in live-cell imaging experiments, PLoS Comput. Biol. 12 (11) (2016) e1005177, http://dx.doi.org/10.1371/journal.pcbi.1005177.
[38] J. Lojk, U. Čibej, D. Karlaš, L. Šajn, M. Pavlin, Comparison of two automatic cell-counting solutions for fluorescent microscopic images, J. Microsc. 260 (2015) 107–116, http://dx.doi.org/10.1111/jmi.12272.
[39] J. Selinummi, P. Ruusuvuori, I. Podolsky, A. Ozinsky, E. Gold, O. Yli-Harja, A. Aderem, I. Shmulevich, Bright field microscopy as an alternative to whole cell fluorescence in automated analysis of macrophage images, PLoS One 4 (2009), http://dx.doi.org/10.1371/journal.pone.0007497.
[40] S. Mohapatra, D. Patra, S. Satpathi, Image analysis of blood microscopic images for acute leukemia detection, IEEE Int. Conf. Ind. Electron. Control Robot (2010) 215–219, http://dx.doi.org/10.1109/IECR.2010.5720171.
[41] N. Patel, A. Mishra, Automated leukaemia detection using microscopic images, Procedia Comput. Sci. (2015) 635–642, http://dx.doi.org/10.1016/j.procs.2015.08.082.
[42] N. Ghane, A. Vard, A. Talebi, P. Nematollahy, Segmentation of white blood cells from microscopic images using a novel combination of K-means clustering and modified watershed algorithm, J. Med. Signals Sens. 7 (2) (2017) 92.
[43] D. Lin, L. Sun, K.A. Toh, J.B. Zhang, Z. Lin, Biomedical image classification based on a cascade of an SVM with a reject option and subspace analysis, Comput. Biol. Med. 96 (2018) 128–140, http://dx.doi.org/10.1016/j.compbiomed.2018.03.005.
[44] G. Wang, Y. Wang, H. Li, X. Chen, H. Lu, Y. Ma, C. Peng, Y. Wang, L. Tang, Morphological background detection and illumination normalization of text image with poor lighting, PLoS One 9 (11) (2014) e110991, http://dx.doi.org/10.1371/journal.pone.0110991.
[45] L. Yang, R. Parton, G. Ball, Z. Qiu, A.H. Greenaway, I. Davis, W. Lu, An adaptive non-local means filter for denoising live-cell images and improving particle detection, J. Struct. Biol. 172 (2010) 233–243, http://dx.doi.org/10.1016/j.jsb.2010.06.019.
[46] S. Basu, S. Kolouri, G.K. Rohde, Detecting and visualizing cell phenotype differences from microscopy images using transport-based morphometry, Proc. Natl. Acad. Sci. 111 (2014) 3448–3453, http://dx.doi.org/10.1073/pnas.1319779111.
[47] I. Guyon, J. Weston, S. Barnhill, V. Vapnik, Gene selection for cancer classification using support vector machines, Mach. Learn. 46 (2002) 389–422, http://dx.doi.org/10.1023/A:1012487302797.
[48] Y. Xue, Z.R. Li, C.W. Yap, L.Z. Sun, X. Chen, Y.Z. Chen, Effect of molecular descriptor feature selection in support vector machine classification of pharmacokinetic and toxicological properties of chemical agents, J. Chem. Inf. Comput. Sci. 44 (5) (2004) 1630–1638, http://dx.doi.org/10.1021/ci049869h.
[49] C.L. Huang, C.J. Wang, A GA-based feature selection and parameters optimizationfor support vector machines, Expert Syst. Appl. 31 (2) (2006) 231–240, http://dx.doi.org/10.1016/j.eswa.2005.09.024.
[50] B. Heisele, T. Serre, S. Prentice, T. Poggio, Hierarchical classification and feature reduction for fast face detection with support vector machines, Pattern Recognit. 36 (9) (2003) 2007–2017, http://dx.doi.org/10.1016/S0031-3203(03)00062-1.
[51] K. İçöz, Image processing and cell phone microscopy to analyze the immunomagnetic beads on micro-contact printed gratings, Appl. Sci. 6 (2016) 279, http://dx.doi.org/10.3390/app6100279.